Quantum Coherence of Rare-Earth Ions in Heterogeneous Photonic Interfaces

Henry C. Hammer,[†] Hassan A. Bukhari,[†] Yogendra Limbu,[†] Brett M. Wasick,[†] Christopher Rouleau,[‡] Michael E. Flatté,^{†,¶} Durga Paudyal,^{*,†} Denis R. Candido,^{*,†} and Ravitej Uppu^{*,†}

†Department of Physics & Astronomy, The University of Iowa, Iowa City, IA 52242 ‡Center for Nanophase Materials Sciences, Oak Ridge National Laboratory, Oak Ridge, Tennessee 37831, USA

 \P Department of Applied Physics, Eindhoven University of Technology, Eindhoven, The Netherlands

E-mail: durga-paudyal@uiowa.edu; denis-candido@uiowa.edu; ravitej-uppu@uiowa.edu

Abstract

Harnessing rare-earth ions in oxides for quantum networks requires integration with bright emitters in III-V semiconductors, but local disorder and interfacial noise limit their optical coherence. Here, we investigate the microscopic origins of the ensemble spectrum in Er^{3+} : TiO_2 epitaxial thin films on GaAs and GaSb substrates. Ab initio calculations combined with noise-Hamiltonian modeling and Monte Carlo simulations quantify the effects of interfacial and bulk spin noise and local strain on erbium crystal-field energies and inhomogeneous linewidths. Photoluminescence excitation spectroscopy reveals that Er^{3+} ions positioned at increasing distances from the III-V/oxide interface produce a systematic blue shift of the $Y_1 \rightarrow Z_1$ transition, consistent with strain relaxation predicted by theory. Thermal annealing produces a

compensating redshift and linewidth narrowing, isolating the roles of oxygen-vacancy and gallium-diffusion noise. These results provide microscopic insight into disorder-driven decoherence, offering pathways for precise control of hybrid quantum systems for scalable quantum technologies.

Quantum network architectures increasingly rely on solid-state quantum memories coupled to photon emitters. ^{1–4} Rare-earth ions (REIs) in crystalline oxides offer exceptional optical and spin coherence because their intra-4f transitions are well shielded from the host lattice. ^{5–7} In particular, Er³⁺ provides telecom-band transitions compatible with existing fiber networks, while III-V semiconductors supply bright, deterministic photon sources and scalable nanophotonic platforms. ^{8,9} Integrating these material classes enables hybrid quantum nodes ¹⁰ that combine scalable photonic circuitry with coherent spin-photon interfaces. ^{11,12} Recent demonstrations of epitaxial Er³⁺:TiO₂ on Si^{13–16} and III-V¹⁷ substrates have extended previous results in a bulk crystal environment, ¹⁸ establishing a promising route toward such hybrid quantum architectures.

Maximizing optical coupling between REIs and photonic modes in hybrid photonic integrated circuits requires positioning REIs within tens of nanometers of the heterovalent oxide/III-V interface. ^{19,20} Its interfacial lattice and valence mismatches create strain and promote cation interdiffusion, leading to local electric- and magnetic-field fluctuations and ultimately limiting REI coherence. ^{19,21} Understanding the microscopic origin and spatial dependence of such noise is, therefore, essential for optimizing hybrid quantum systems. While decoherence mechanisms in bulk or implanted crystals have been studied extensively, ^{22–24} there is a critical need to understand interfaces of heteroepitaxial films and the interplay between interfacial and bulk noise sources.

Here, we develop a microscopic theoretical-experimental framework linking interfacial chemistry to optical decoherence in Er^{3+} :TiO₂ thin films grown on Ga-based substrates. By combining photoluminescence-excitation spectroscopy of δ -doped films with noise modeling and *ab initio* crystal-field calculations, we quantify how gallium diffusion, oxygen-vacancy

gradients, and strain collectively shape the spectral response of ensembles of Er^{3+} ions. This unified description connects local and ensemble linewidth physics within a single parameter set and provides quantitative guidelines for designing coherent oxide/semiconductor heterostructures that host rare-earth ions.

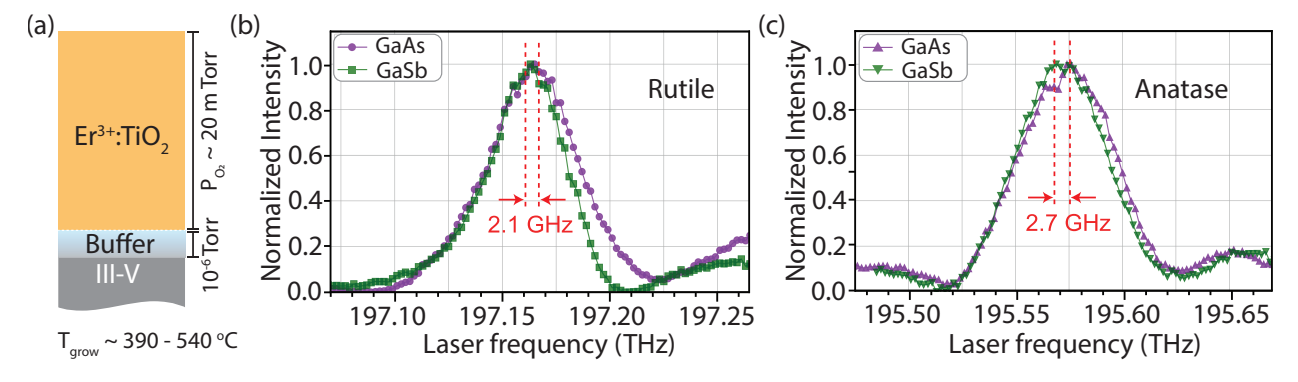


Figure 1: (a) Schematic of the synthesized heteroepitaxial Er^{3+} : TiO_2 thin film on III-V substrates featuring an undoped buffer layer grown under high vacuum. Photoluminescence excitation (PLE) spectra of the $Y_1 \to Z_1$ transition in Er^{3+} doped into the rutile (b) and anatase (c) phase thin films grown on GaAs and GaSb substrates.

 ${\rm Er}^{3+}$ -doped TiO₂ thin films were grown on GaAs and GaSb substrates by pulsed laser deposition. TiO₂ provides a model system for probing REI optical coherence owing to its wide bandgap transparency, minimal host nuclear spin density, and established low-temperature epitaxy on GaAs and GaSb. ¹⁷ Figure 1(a) schematically illustrates the heterogeneous film geometries featuring a thin, undoped TiO₂ buffer ($\approx 1-5$ nm) grown under high vacuum and a 3000 ppm Er-doped film of 60-90 nm thickness grown in an oxygen ambient pressure of 20 mTorr. Growth temperature and surface-preparation conditions determine whether rutile (R) or anatase (A) polymorphs form. R-TiO₂ films grown on GaAs(100) develop mixed (110)/(210) orientations that partially relax strain, whereas growth on GaSb(100) yields a (200) orientation with an estimated interfacial compressive strain of 0.48%, based on minimal coincident interface area calculations. In contrast, A-TiO₂ films grow with (001) orientation on both GaAs(100) and GaSb(100) substrates, exhibiting biaxial in-plane compressive strains of 0.43% and 0.12%, respectively. ¹⁷ The sensitivity of TiO₂ polymorphs to substrate lattice mismatch thus enables strain engineering through substrate selection,

offering a controllable handle on interfacial stress and defect formation. These distinct strain states make the $A-TiO_2/III-V$ system an ideal platform for probing how lattice mismatch and interface chemistry influence the REI optical spectra.

Elements of the optical response of Er^{3+} doped into TiO_2 thin films can be predicted using crystal field calculations. We compute 25 crystal-field coefficients (CFCs) using large supercells containing a single Er^{3+} substituting a Ti^{4+} , corresponding to a 1.389% doping concentration in both rutile ($3 \times 3 \times 4$ supercell) and anatase ($3 \times 3 \times 2$ supercell) polymorphs. The CFCs are extracted 25 from the crystal-field potential obtained using non-spin-polarized density-functional theory (DFT) using the 4f-core approximation 26 and dielectric constants of 2.00 (rutile) 25 and 2.231 (anatase), 25,27 which are required for determining the 4f energy levels. These coefficients serve as inputs to an effective Hamiltonian solved using the qlanth code, yielding the Er^{3+} 4f energy spectrum. 28,29 Epitaxial strain lowers the local Er site symmetry in the ideal lattice from D_{2h} to C_{2h} in rutile and from D_{2d} to C_s in anatase on both (GaAs and GaSb) substrates. This results in nine non-zero CFC (B_q^k) terms, leading to eight Z_1 - Z_8 ground-state and seven Y_1 - Y_7 first-excited-state doublets (see Supplemental Material). DFT computations predict characteristic dependences of the level splitting on the presence of local defects (e.g., oxygen vacancies) and strain relaxation, as will be discussed later.

Figures 1(b,c) show photoluminescence excitation (PLE) spectra measured at 5 K, high-lighting the characteristic shift in the $Y_1 \rightarrow Z_1$ transition between the two polymorphs: 197.165 GHz (1520.5 nm) on R-TiO₂ and 195.575 GHz (1532.9 nm) on A-TiO₂. Growth on different substrates further shifts the $Y_1 \rightarrow Z_1$ transition by about 2.5 GHz, in good agreement with the predictions from crystal-field calculations (see Supplemental Material). The R-TiO₂ film grown on GaSb exhibits a more pronounced asymmetric lineshape than that on GaAs. Although A-TiO₂ experiences different absolute strain levels than R-TiO₂, the fractional change in strain between films grown on GaSb and GaAs is comparable, as reflected by similar frequency shifts. Despite this, the measured PLE spectra are more sym-

metric and exhibit a slightly narrower inhomogeneous linewidth on GaSb ($49\pm1~\mathrm{GHz}$) than on GaAs ($53\pm1~\mathrm{GHz}$). Such substrate-dependent asymmetry and linewidth variations indicate that multiple factors, such as strain, intermixing, and vacancies, act concurrently to modify the local environment of Er³⁺ ions near the oxide/III-V interface. These effects are expected to vary spatially across the film thickness and ultimately influence the measured optical lineshapes.

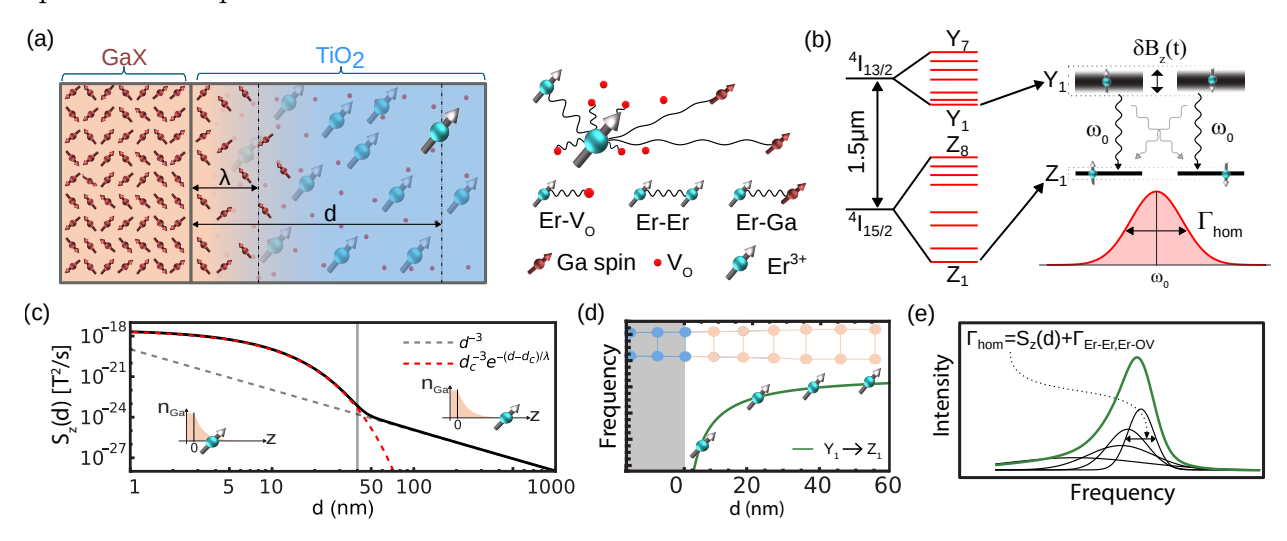


Figure 2: (a) Schematic of the GaX-TiO₂ heterostructure indicating Er ions (cyan) at interfacial distance d that interact with Ga spins (brown) that diffuse into TiO₂ with characteristic length λ and oxygen vacancies (red) $V_{\rm O}$. (b) Illustration of linewidth broadening arising from the fluctuating magnetic fields $\delta B_z(t)$ on the $Y_1 \to Z_1$ transition of the crystal-field-split energy levels of Er³⁺. (c) Spectral noise density $S_z(d)$ due to Ga nuclear spins as a function of distance d, compared to the expected d^{-3} (gray dashed) and $d_c^{-3}e^{-(d-d_c)/\lambda}$ (red dotted) dependencies with $\lambda=4$ nm and $d_c=0.35$ nm. Insets show a schematic of Ga spin density distributions near and far from the interface. (d) Distance-dependent $Y_1 \to Z_1$ transition frequency $\omega(d)$, illustrating the influence of interfacial strain. (e) Illustration of the asymmetric inhomogeneous lineshape resulting from the interplay between strain and distance-dependent individual Er³⁺ homogeneous linewidths.

Figure 2 summarizes how interfacial intermixing, point defects, and strain jointly influence the Er^{3+} optical transitions and determine the measured inhomogeneous linewidth. These factors not only broaden the homogeneous linewidth Γ_{hom} of individual ions but also induce static or dynamic frequency shifts that vary with the interfacial distance d. The resulting noise environment includes interactions of Er^{3+} with Ga, oxygen vacancies (V_O), and other Er ions, as indicated in Fig. 2(a). Interfacial intermixing, wherein gallium atoms from the substrate diffuse into the oxide lattice over a characteristic diffusion length λ , perturbs the local electrostatic potential while simultaneously introducing both nuclear spins and unpaired electronic spins and associated noise. Oxygen vacancies are formed predominantly during growth due to limited adatom mobility at the relatively low substrate temperatures (< 400 °C) and the non-equilibrium plasma plume kinetics. $V_{\rm O}$ occupation dynamics generate fluctuating electric and magnetic fields that drive charge- and spin-state fluctuations of nearby Er³⁺ ions. ^{15,30-33} In addition, the relatively high Er concentration (~3000 ppm) produces strong dipolar Er–Er interactions that contribute to spectral diffusion and define a baseline inhomogeneous linewidth. ^{15,22,33}

Near the heterovalent interface, a significant contribution to the Er³⁺ linewidth arises from the electromagnetic noise generated by Ga atoms. Within a few nanometers of the interface, the Er³⁺ ions reside in a dense bath of Ga impurities, whose nuclear spins produce slowly fluctuating magnetic fields, leading to substantial broadening of the Er³⁺ transitions. Although Ga atoms migrating into TiO₂ could form paramagnetic centers, such configurations are expected to be extremely rare. In TiO₂, Ga³⁺ predominantly substitutes on the Ti⁴⁺ site, and charge compensation via nearby oxygen vacancies drives the resulting Ga-V_O complexes towards closed-shell electronic configurations that do not host unpaired electrons. ^{34,35} Any transient electron-spin centers that may form under non-equilibrium interfacial conditions would possess large dipole moments and therefore couple strongly to their environment, leading to nanosecond or faster spin-fluctuation dynamics, ³⁶ far shorter than the correlation time of nuclear spins. ^{37,38} Consequently, such a dilute concentration of rapidly fluctuating electron-spin noise results in a negligible contribution to the Er³⁺ linewidth. For these reasons, and as discussed further in Supplemental Material, we neglect the contribution of Ga-related unpaired electrons in the linewidth analysis.

Far from the interface, the local Ga nuclear-spin bath becomes increasingly dilute, allowing it to be treated as a remote, fluctuating three-dimensional spin bath. To describe this effect, we model the position-dependent spectral noise density, $S_z(d)$, and the corresponding

linewidth broadening $\Gamma_{\text{Ga}}(d) = \gamma_{\text{Er}}^2 S_z(d)/\pi$ with γ_{Er} the gyromagnetic ratio of Er ions, as illustrated in Fig. 2(b) (see Supplemental Material). For distances $d \gg \lambda$, the noise follows the dipolar scaling $S_z(d) \propto n_{\text{Ga}}/d^3$, where n_{Ga} is the density of the three-dimensional bath of Ga nuclear spins of the substrate. ^{39,40} For $d \gtrsim \lambda$, the distance dependence transitions to $S_z(d) \propto n_{\text{Ga}} e^{-(d-d_c)/\lambda}/d_c^3$, where d_c corresponds to the shortest Ti-Ti separation in TiO₂ and defines the minimum possible distance between a diffused Ga atom and an Er³⁺ ion (Fig. 2(c)). This exponential attenuation captures the rapid rise of magnetic noise near the interface and its gradual decay into the film interior, deviating strongly from the $1/d^3$ behavior expected for purely bulk spin noise (gray dashed line).

In addition to magnetic and defect-related noise, local strain plays a central role in shaping the optical response. As shown schematically in Figure 2(d), interfacial lattice mismatch introduces compressive strain that relaxes with increasing distance from the interface, leading to position-dependent Stark shifts of the Er crystal-field levels. When position-dependent frequencies and linewidths coexist, the ensemble spectrum can acquire an intrinsic asymmetry. This interplay, visualized in Figure 2(e), provides a microscopic origin for the asymmetric lineshapes observed in Figure 1(b,c) and motivates a spatially resolved investigation of the underlying strain and noise fields.

We synthesized pseudo- δ -doped TiO₂ films containing a narrow (2 nm) Er-doped layer positioned at a controlled distance from the GaAs/TiO₂ interface, as illustrated in Figure 3(a). These δ -doped structures isolate a well-defined spatial slice of the strain and intermixing profiles, enabling direct correlation between local environment and optical response. We focus on A-TiO₂ grown on GaAs because this combination yielded the most reproducible crystalline quality, sub-nm surface roughness, and short Ga diffusion length ($\lambda \approx 4$ nm) under the low growth temperatures ($<400^{\circ}$ C) required for rare-earth incorporation. ¹⁷ While similar epitaxy on GaSb is feasible, the narrower process window and higher volatility of Sb make GaAs a more robust substrate for controlled interfacial chemistry and strain engineering using pulsed laser deposition. We investigated the optical properties of the δ -doped samples

before and after annealing (4 h at 450°C in air) to probe the influence of oxygen vacancies. ³³

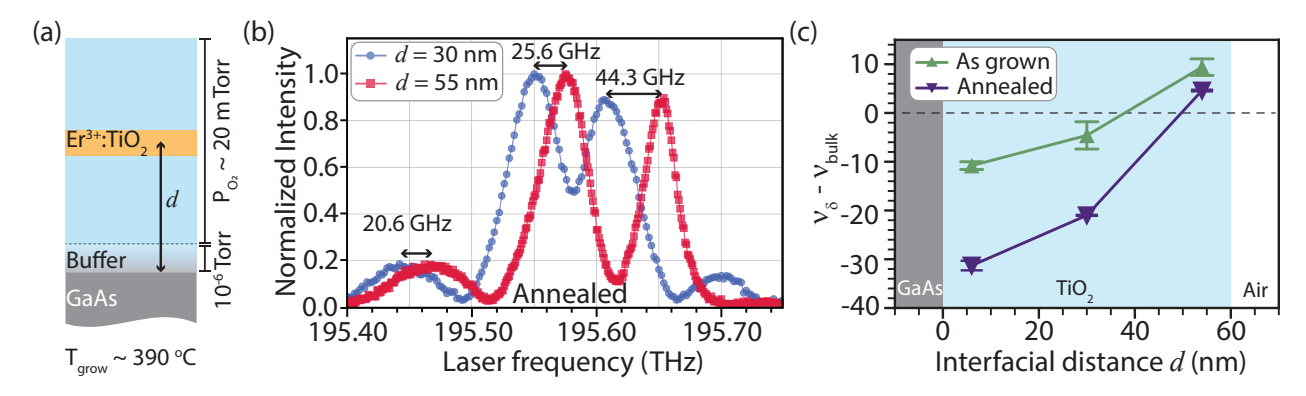


Figure 3: (a) Schematic of the selectively-doped Er^{3+} :TiO₂ thin film on GaAs featuring a 2 nm-thin doped layer introduced at an interfacial distance d. (b) PLE spectra around the $Y_1 \to Z_1$ transition of Er^{3+} ions in such annealed thin films exhibit significant frequency shifts due to distance-dependent strain in the thin film. (c) Frequency shift of the $Y_1 \to Z_1$ transition (ν_{δ}) before and after annealing, relative to the measured frequency in uniformly-doped samples (ν_{bulk}) , highlights the interplay between strain and oxygen-vacancy contributions.

PLE spectra of annealed samples with Er^{3+} doped at two interfacial distances, d=30 and 55 nm, are shown in Figure 3(b). The spectra feature three prominent peaks, with the central one corresponding to the $Y_1 \to Z_1$ transition that blueshifts by 25.6 GHz with increasing d. Furthermore, distinct blueshifts are observed for peaks corresponding to different crystal-field-split transitions, in agreement with ab initio computations (see Supplemental Material). The distance-dependent frequency shift $\nu_{\delta}(d)$, plotted in Figure 3(c) before and after annealing, follows a quadratic dependence. After annealing, we observe a steeper relative shift in $\nu_{\delta}(d)$, potentially signaling increased interfacial strain from additional Ga diffusion. Additionally, a slight redshift of 5 GHz is observed between the annealed and as-grown samples far from the interface (d=55 nm), which potentially arises from the annihilation of $V_{\rm OS}$ as demonstrated via simulations of reaction-diffusion model (see Supplemental Material).

The microscopic origin of the distance-dependent frequency shifts was predicted by DFT for Er-doped rutile and anatase TiO_2 , both with and without nearby oxygen vacancies. First, we compute how biaxial strain modifies the crystal-field splitting and transition energies of Er^{3+} in A-TiO₂ without V_O . Using the experimentally determined out-of-plane (c-axis) strain of -1% (compressive) from X-ray diffraction measurements, we varied the in-plane biaxial

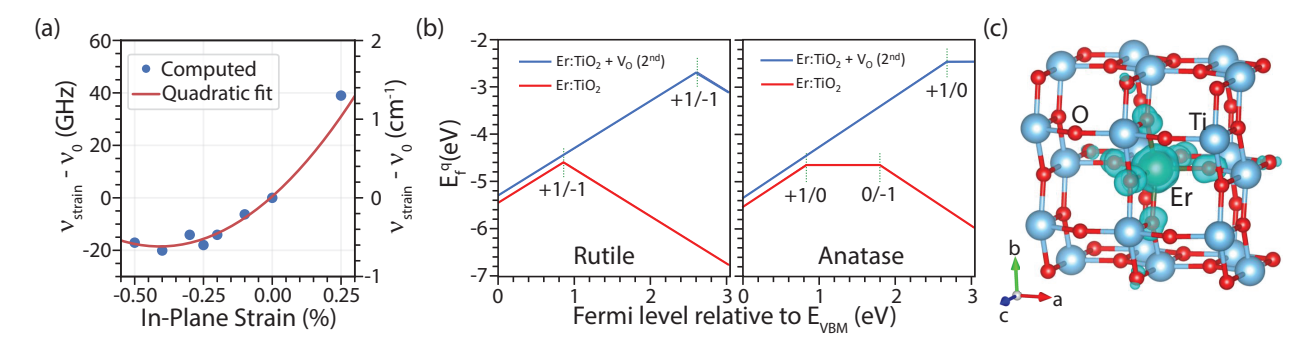


Figure 4: (a) Effect of in-plane compressive and tensile strain (with 1% fixed c-axis compression) on crystal field energy levels. (b) Defect formation energy of Er-doped TiO₂ with (blue) and without (red) V_O at the next nearest neighbor. (c) Spin density of neutral Er-doped A-TiO₂ (q = 0). The large spin density on Er arises from its $\sim 3 \mu_B$ spin moment (Er³⁺), while nearby O atoms show small induced spin densities due to Er-4f and O-2p hybridization (see Supplemental Material).

strain uniformly between compressive and tensile values. Figure 4(a) reveals that relaxing from an in-plane compressive strain of -0.45% (consistent with epitaxial conditions) to zero strain produces a 20 GHz blueshift of the $Y_1 \rightarrow Z_1$ transition, in close agreement with the δ -doped measurements (Figure 3(c)). The computed strain-dependent frequency shift in Fig. 4(a) exhibits a quadratic dependence for small strains ($\pm 0.5\%$). Minor changes in out-of-plane strain after annealing may account for the slightly broader frequency range observed experimentally in Figure 3(c). Because the DFT-calculated frequency variation with strain and the measured frequency shift with interfacial distance (Figure 3(c)) are both quadratic, we conclude that the in-plane strain relaxes linearly with d. This correspondence both reinforces our experimental observation and provides a physically grounded model for distance-dependent frequency shift as:

$$\omega_{\text{strain}}(d) \sim \omega_0 - ad^2.$$
 (1)

Alongside strain, charge-state compensation arising from Er^{3+} substituting for Ti^{4+} and the stability of associated V_O defects govern the local crystal-field environment, influencing both the transition frequencies and linewidth broadening.⁴¹ When a first-shell (nearest-neighbor) oxygen vacancy is introduced in R-TiO₂, the Er^{3+} local site symmetry reduces

to C_1 from C_{2h} , resulting in fifteen non-zero B_q^k values and a relatively large 4f splitting compared to experiments. Consequently, second-shell vacancies that result in C_s site symmetry with nine non-zero \mathcal{B}_q^k values were considered as more representative of the measured spectra. The computed crystal-field coefficients (B_q^k) and resulting intra-4f level energies for both R-TiO $_2$ and A-TiO $_2$ are discussed in detail in Supplemental Material. $V_{\rm O}$ defectformation-energy calculations (Figure 4(b)) reveal different charge compensation behavior in rutile and anatase TiO_2 . The formation energy of a defect in charge state q was computed as $E_{\rm f}^{\rm q}(\epsilon_{\rm F}) = E_{ds}^q - E_{ps}^q + \sum_i n_i \mu_i + q(E_{\rm VBM} + \epsilon_{\rm F}) + E_{\rm corr}$, where E_{ds}^q (E_{ps}^q) is the total energy of the defective (pristine) supercell, μ_i the chemical potentials at site $i, n_i = 1$ (-1) for an added (removed) i^{th} atom, E_{VBM} the valence band maxima, ϵ_{F} the Fermi energy, and E_{corr} the electrostatic and image-charge corrections. 42 In R-TiO₂, isolated Er favors a q=-1charge state at mid-gap, but the presence of a $V_{\rm O}$ at the second shell stabilizes the q=+1configuration up to a Fermi energy of 2.615 eV. The neutral state (q = 0) is unstable, indicating a preference for local charge compensation through proximal $V_{\rm O}$ that enhances local electric- or magnetic-field fluctuations and reduces optical coherence. In contrast, Er-doped A-TiO₂ favors a neutral (q = 0) charge state, with the q = +1 appearing only when a $V_{\rm O}$ is introduced nearby, highlighting non-local charge compensation through the extended oxygen network as seen in Figure 4(c). These charge-state differences modulate the crystal-field coefficients and the 4f-level splitting (see Supplementary Material), while changes in their occupation lead to charge noise that determines linewidth broadening.

Having established that Ga intermixing (Figure 2), strain relaxation, and vacancy-mediated charge compensation jointly define the local environment of Er^{3+} , we now quantify their combined impact on the optical linewidths. Figure 5(a) presents the distance-dependent inhomogeneous linewidth of the $Y_1 \to Z_1$ transition obtained from A-TiO₂/GaAs δ -doped samples. Before annealing, the linewidths remain broad ($\approx 50 \text{ GHz}$) and nearly independent of d, indicating that charge- and spin-noise contributions from V_0 and Er-Er interactions dominate. After annealing, the linewidth decreases with d, consistent with prior reports of

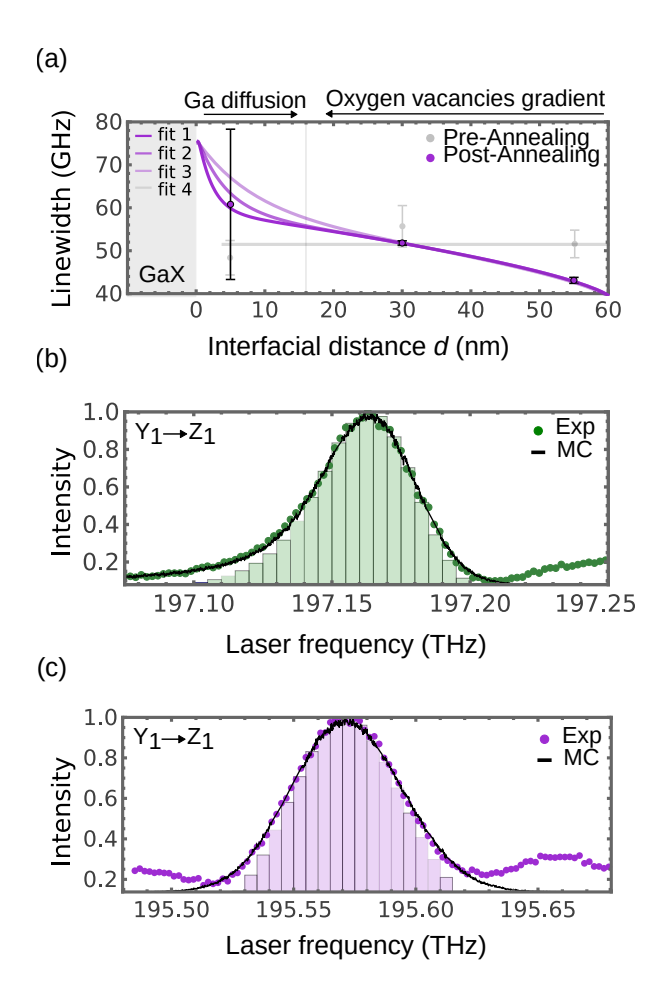


Figure 5: (a) Inhomogeneous linewidth Γ_{inh} as a function of distance from GaX-TiO₂ interface before and after annealing of the δ -doped A-TiO₂ samples. (b) Experimental and simulated lineshape for the $Y_1 \to Z_1$ transition in A – TiO₂. (c) Experimental and Monte Carlo-simulated lineshape for the $Y_1 \to Z_1$ transition in R – TiO₂.

TiO₂ films on silicon, ¹⁵ but two distinct regimes emerge. Far from the interface, the linewidth decreases by about 8 GHz relative to as-grown films, reflecting the annihilation of $V_{\rm O}$ centers that promote local charge compensation and broaden linewidth due to excess charge-noise. Because the magnetic-noise spectral density $S_z(d)$ arising from Ga nuclei is more than six orders of magnitude smaller at this distance, the linewidth is then primarily limited by dipolar Er–Er interactions, yielding $\Gamma_{\text{Er-Er}} \approx 42$ GHz. Closer to the interface (d < 20 nm), the linewidth broadens by at least 10 GHz after annealing. This excess broadening indicates increased gallium diffusion into the TiO₂ lattice during thermal annealing, which introduces additional electromagnetic noise that outweighs the reduction in $V_{\rm O}$ -related noise. Er³⁺ ions situated within this interfacial distance also experience a forced electric dipole moment, consistent with a measured excited-state lifetime of 0.2(1) ms (see Supplemental Material). The resulting increased sensitivity of charge- and spin-noise leads to fluorescence quenching that significantly weakens the PLE signal near the interface, even at the high Er concentrations (3000 ppm) employed in our measurements. The low activation energy for Ga diffusion (≈ 2.5 eV; diffusion constant $\approx 10^{-17} \text{ cm}^2 \text{ s}^{-1}$) previously measured for PLD-grown films facilitates this enhanced intermixing, confirming that interfacial Ga spins dominate the post-anneal dephasing environment.

To model these trends quantitatively, we assume a $V_{\rm O}$ -density gradient, based on reaction-diffusion modeling, that linearly decreases with d, i.e., $n_{V_{\rm O}}(d) \propto d$. Whether originating from spin or charge noise, the corresponding contribution of $V_{\rm O}$ centers to linewidth is $\Gamma_{V_{\rm O}}(d) = b n_{V_{\rm O}}^{2/3}(d)$, 31,33 where b represents the coupling constant for the underlying noise mechanism. The resulting total linewidth is $\Gamma(d) = \Gamma_{\rm Er-Er} + \Gamma_{V_{\rm O}}(d) + \Gamma_{\rm Ga}(d)$. This analytical form quantitatively reproduces the experimental data in Figure 5(a), showing that $V_{\rm O}$ - and Er–Errelated noise dominate at large d, while Ga-spin noise controls the linewidth for $d \lesssim \lambda$. The larger uncertainties near the interface likely arise from spatially nonuniform Ga diffusion and reduced signal-to-noise ratios due to fluorescence quenching.

Using this distance-resolved linewidth $\Gamma(d)$ together with the strain-induced frequency

shift $\omega_{\text{strain}}(d)$, we performed Monte Carlo simulations to model the ensemble spectrum of uniformly-doped A-TiO₂/GaAs film shown in Figure 1(c). Sampling a million Er³⁺ ions with random spatial positions d_i within the TiO₂ layer, the simulations reproduce the lineshape observed experimentally (Figure 5(b)). Applying the same model to the R-TiO₂ grown on GaSb, while adjusting only $\omega_{\text{strain}}(d) = \omega - c/d$, captures the broader, more asymmetric spectrum characteristic of that heterostructure (Figure 5(c)). These results demonstrate that a single microscopic framework quantitatively accounts for both strain-driven frequency shifts and noise-limited linewidth broadening across TiO₂/III-V interfaces.

Our work establishes a unified microscopic picture that connects interfacial chemistry, strain, and defect dynamics to the optical response of Er³⁺ in TiO₂/III–V heterostructures. By integrating δ -doped spectroscopy, ab initio calculations, noise Hamiltonian modeling, and Monte Carlo simulations, we directly link interfacial structure to ensemble optical behavior. The analysis shows that interfacial Ga spins dominate dephasing and linewidth near the oxide/III-V boundary, whereas oxygen-vacancy and Er-Er interactions govern broadening deeper in the film. The modeling further predicts that the stronger coupling between strain and cation intermixing expected in rutile TiO₂ on GaSb results in broader, more asymmetric spectra than those of the anatase TiO₂ on GaAs system studied experimentally. This unified framework quantitatively reproduces linewidth values and both symmetric and asymmetric lineshapes, providing a predictive tool for designing low-decoherence REI/semiconductor interfaces. Future studies employing two- and three-pulse photon-echo measurements under small external magnetic fields ($B \sim 100$ mT) can directly probe the homogeneous linewidth (T_2) and spectral-diffusion dynamics as a function of Er-ion distance from the III-V interface. Such experiments would extend the framework developed here to quantify decoherence processes at the single-ion level and guide the design of scalable hybrid quantum architectures.

Acknowledgement

R.U. acknowledges funding from the National Science Foundation (NSF) under the CA-REER program (ECCS2339469) and a seed grant from the University of Iowa's Office of the Vice President for Research through the P3 Jumpstarting Tomorrow program. Ab initio crystal field calculations, defect formation energies, noise-Hamiltonian modeling, and noise simulations were supported by the U.S. Department of Energy, Office of Science, Office of Basic Energy Sciences under Award Number DE-SC0023393. Target fabrication and pulsed laser deposition were conducted as part of a user project (CNMS2023-B-02072) at the Center for Nanophase Materials Sciences (CNMS), which is a US Department of Energy, Office of Science User Facility at Oak Ridge National Laboratory.

References

- (1) Wehner, S.; Elkouss, D.; Hanson, R. Quantum internet: A vision for the road ahead. Science 2018, 362, eaam9288.
- (2) Azuma, K.; Economou, S. E.; Elkouss, D.; Hilaire, P.; Jiang, L.; Lo, H.-K.; Tzitrin, I. Quantum repeaters: From quantum networks to the quantum internet. Rev. Mod. Phys. 2023, 95, 045006.
- (3) Atatüre, M.; Englund, D.; Vamivakas, N.; Lee, S.-Y.; Wrachtrup, J. Material platforms for spin-based photonic quantum technologies. *Nat. Rev. Mater.* **2018**, *3*, 38–51.
- (4) Awschalom, D. D.; Hanson, R.; Wrachtrup, J.; Zhou, B. B. Quantum technologies with optically interfaced solid-state spins. *Nat. Photonics* **2018**, *12*, 516–527.
- (5) Thiel, C.; Böttger, T.; Cone, R. Rare-earth-doped materials for applications in quantum information storage and signal processing. *J. Lumin.* **2011**, *131*, 353–361.

- (6) Zhong, T.; Goldner, P. Emerging rare-earth doped material platforms for quantum nanophotonics. *Nanophotonics* **2019**, *8*, 2003–2015.
- (7) Goldner, P.; Tallaire, A.; Serrano, D.; Tiranov, A.; Zhong, T. Rare-Earth Doped Thin Films for Optical Quantum Technologies. *Advanced Quantum Technologies* e2500026.
- (8) Uppu, R.; Pedersen, F. T.; Wang, Y.; Olesen, C. T.; Papon, C.; Zhou, X.; Midolo, L.; Scholz, S.; Wieck, A. D.; Ludwig, A.; Lodahl, P. Scalable integrated single-photon source. *Sci. Adv.* **2020**, *6*, eabc8268.
- (9) Tomm, N.; Javadi, A.; Antoniadis, N. O.; Najer, D.; Löbl, M. C.; Korsch, A. R.; Schott, R.; Valentin, S. R.; Wieck, A. D.; Ludwig, A.; Warburton, R. J. A bright and fast source of coherent single photons. *Nat. Nanotechnol.* 2021, 16, 399–403.
- (10) Strocka, Y.; Gu, F.; Pieplow, G.; Borregaard, J.; schröder, T. Hybrid Quantum Repeater Chains with Semiconductor Quantum Dots and Group-IV-Vacancy Color Centers in Diamond. 2025; https://arxiv.org/abs/2511.02472.
- (11) Uppu, R.; Midolo, L.; Zhou, X.; Carolan, J.; Lodahl, P. Quantum-dot-based deterministic photon–emitter interfaces for scalable photonic quantum technology. *Nat. Nanotechnol.* 2021, 16, 1308–1317.
- (12) Yu, Y.; Liu, S.; Lee, C.-M.; Michler, P.; Reitzenstein, S.; Srinivasan, K.; Waks, E.; Liu, J. Telecom-band quantum dot technologies for long-distance quantum networks.

 Nat. Nanotechnol. 2023, 18, 1389–1400.
- (13) Dibos, A. M.; Solomon, M. T.; Sullivan, S. E.; Singh, M. K.; Sautter, K. E.; Horn, C. P.; Grant, G. D.; Lin, Y.; Wen, J.; Heremans, F. J.; Guha, S.; Awschalom, D. D. Purcell Enhancement of Erbium Ions in TiO₂ on Silicon Nanocavities. *Nano Lett.* 2022, 22, 6530–6536.

- (14) Ji, C.; Solomon, M. T.; Grant, G. D.; Tanaka, K.; Hua, M.; Wen, J.; Seth, S. K.; Horn, C. P.; Masiulionis, I.; Singh, M. K.; Sullivan, S. E.; Heremans, F. J.; Awschalom, D. D.; Guha, S.; Dibos, A. M. Nanocavity-Mediated Purcell Enhancement of Er in TiO₂ Thin Films Grown via Atomic Layer Deposition. ACS Nano 2024, 18, 9929–9941.
- (15) Singh, M. K.; Grant, G. D.; Wolfowicz, G.; Wen, J.; Sullivan, S. E.; Prakash, A.; Dibos, A. M.; Joseph Heremans, F.; Awschalom, D. D.; Guha, S. Optical and microstructural studies of erbium-doped TiO₂ thin films on silicon, SrTiO₃, and sapphire. J. Appl. Phys. 2024, 136, 124402.
- (16) Pettit, R. M.; Deckoff-Jones, S.; Donis, A.; Elias, A.; Briscoe, J.; Leake, G.; Coleman, D.; Fanto, M.; Sundaresh, A.; Gupta, S.; Singh, M. K.; Sullivan, S. E. Monolithically Integrated C-Band Quantum Emitters on Foundry Silicon Photonics. *Nano Lett.* 2025, 25, 11803–11810.
- (17) Hammer, H. C.; Whittier, C.; Helvy, N. A.; Rouleau, C.; Bassim, N. D.; Uppu, R. Controlled growth of rare-earth-doped TiO₂ thin films on III-V semiconductors for hybrid quantum photonic interfaces. 2025; https://arxiv.org/abs/2511.03918.
- (18) Phenicie, C. M.; Stevenson, P.; Welinski, S.; Rose, B. C.; Asfaw, A. T.; Cava, R. J.; Lyon, S. A.; de Leon, N. P.; Thompson, J. D. Narrow Optical Line Widths in Erbium Implanted in TiO₂. Nano Letters 2019, 19, 8928–8933.
- (19) Wu, C.-J.; Riedel, D.; Ruskuc, A.; Zhong, D.; Kwon, H.; Faraon, A. Near-infrared hybrid quantum photonic interface for ¹⁷¹Yb³⁺ solid-state qubits. *Phys. Rev. Appl.* **2023**, *20*, 044018.
- (20) Uysal, M. T.; Dusanowski, L.; Xu, H.; Horvath, S. P.; Ourari, S.; Cava, R. J.; de Leon, N. P.; Thompson, J. D. Spin-Photon Entanglement of a Single Er³⁺ Ion in the Telecom Band. *Phys. Rev. X* **2025**, *15*, 011071.

- (21) Ourari, S.; Dusanowski, Ł.; Horvath, S. P.; Uysal, M. T.; Phenicie, C. M.; Stevenson, P.; Raha, M.; Chen, S.; Cava, R. J.; de Leon, N. P.; Thompson, J. D. Indistinguishable telecom band photons from a single Er ion in the solid state. *Nature* **2023**, *620*, 977–981.
- (22) Böttger, T.; Thiel, C. W.; Sun, Y.; Cone, R. L. Optical decoherence and spectral diffusion at 1.5 μm in Er³⁺ : Y₂SiO₅ versus magnetic field, temperature, and Er³⁺ concentration. Phys. Rev. B 2006, 73, 075101.
- (23) Sun, Y.; Böttger, T.; Thiel, C. W.; Cone, R. L. Magnetic g tensors for the ${}^4I_{15/2}$ and ${}^4I_{13/2}$ states of Er³⁺ : Y₂SiO₅. *Phys. Rev. B* **2008**, 77, 085124.
- (24) Böttger, T.; Thiel, C. W.; Cone, R. L.; Sun, Y. Effects of magnetic field orientation on optical decoherence in Er³⁺ : Y₂SiO₅. *Phys. Rev. B* **2009**, *79*, 115104.
- (25) Limbu, Y.; Shi, Y.; Sink, J.; Puel, T. O.; Paudyal, D.; Flatté, M. E. Ab initio calculations of erbium crystal field splittings in oxide hosts: role of the 4f radial wave function. arXiv preprint arXiv:2501.03353 2025,
- (26) Novák, P.; Knížek, K.; Maryško, M.; Jirák, Z.; Kuneš, J. Crystal field and magnetism of Pr³⁺ and Nd³⁺ ions in orthorhombic perovskites. *J. Phys. Condens. Matter* **2013**, 25, 446001.
- (27) Paudyal, H.; Limbu, Y.; Flatté, M. E.; Paudyal, D. Singly occupied 4f antiferromagnetic insulators: CePO₄ and CeVO₄. Phys. Rev. B **2025**, 112, 155112.
- (28) qlanth: A Hamiltonian for the lanthanides. San Francisco (CA): GitHub, 2022; https://github.com/zia-lab/qlanth.
- (29) Lizarazo-Ferro, J.-D.; Puel, T. O.; Flatté, M. E.; Zia, R. Refining spectroscopic calculations for trivalent lanthanide ions: a revised parametric Hamiltonian and open-source solution. arXiv preprint arXiv:2503.17377 2025,

- (30) Linderälv, C.; Lindman, A.; Erhart, P. A Unifying Perspective on Oxygen Vacancies in Wide Band Gap Oxides. *J. Phys. Chem. Lett.* **2017**, *9*, 222–228.
- (31) Candido, D. R.; Flatté, M. E. Suppression of the Optical Linewidth and Spin Decoherence of a Quantum Spin Center in a p-n Diode. *PRX Quantum* **2021**, *2*, 40310.
- (32) Candido, D. R.; Flatté, M. E. Interplay between charge and spin noise in the near-surface theory of decoherence and relaxation of C_{3v} Symmetry qutrit spin-1 centers. Phys. Rev. B **2024**, 110, 24419.
- (33) Grant, G. D. et al. Optical and microstructural characterization of Er³⁺ doped epitaxial cerium oxide on silicon. *APL Mater.* **2024**, *12*, 021121.
- (34) Okajima, T.; Yamamoto, T.; Kunisu, M.; Yoshioka, S.; Tanaka, I.; Umesaki, N. Dilute Ga Dopant in TiO2 by X-ray Absorption Near-Edge Structure. *Jap. J. Appl. Phys.* **2006**, *45*, 7028.
- (35) Gionco, C.; Livraghi, S.; Maurelli, S.; Giamello, E.; Tosoni, S.; Di Valentin, C.; Pacchioni, G. Al- and Ga-Doped TiO2, ZrO2, and HfO2: The Nature of O 2p Trapped Holes from a Combined Electron Paramagnetic Resonance (EPR) and Density Functional Theory (DFT) Study. Chem. Mater. 2015, 27, 3936–3945.
- (36) Wu, Z.; Jiang, M.; Guo, J.; Yang, Q.; Zhang, Y.; Jia, T.; Sun, Z.; Feng, D. Long-lived electron spin coherence in Ga-doped ZnO at room temperature. *Phys. Rev. B* **2021**, 103, L140411.
- (37) Hall, L. T.; Cole, J. H.; Hollenberg, L. C. L. Analytic solutions to the central-spin problem for nitrogen-vacancy centers in diamond. *Phys. Rev. B* **2014**,
- (38) de Sousa, R.; Das Sarma, S. Theory of nuclear-induced spectral diffusion: Spin decoherence of phosphorus donors in Si and GaAs quantum dots. *Phys. Rev. B* **2003**, *68*, 115322.

- (39) Pham, L. M.; DeVience, S. J.; Casola, F.; Lovchinsky, I.; Sushkov, A. O.; Bersin, E.; Lee, J.; Urbach, E.; Cappellaro, P.; Park, H.; Yacoby, A.; Lukin, M.; Walsworth, R. L. NMR technique for determining the depth of shallow nitrogen-vacancy centers in diamond. *Phys. Rev. B* 2016, *93*, 045425.
- (40) Zhang, W.; Zhang, J.; Wang, J.; Feng, F.; Lin, S.; Lou, L.; Zhu, W.; Wang, G. Depth-dependent decoherence caused by surface and external spins for NV centers in diamond. *Phys. Rev. B* **2017**, *96*, 235443.
- (41) Martins, J. B.; Grant, G.; Haskel, D.; Sterbinsky, G. E.; Masiulionis, I.; Sautter, K. E.; Karapetrova, E.; Guha, S.; Freeland, J. W. The role of the dopant in the electronic structure of erbium-doped TiO₂ for quantum emitters. *APL Mater.* **2024**, *12*, 121110.
- (42) Limbu, Y.; Paudyal, H.; Flatté, M. E.; Paudyal, D. Stability, electronic quantum states, and magnetic interactions of Er³⁺ ions in Ga₂O₃. arXiv preprint arXiv:2503.12194 **2025**,